14th International Symposium on Turbulence and Shear Flow Phenomena (TSFP14)
Heidelberg, Germany, July 28–31, 2026

TURBULENT CHANNEL FLOW WITH COHESIVE PARTICLES

Alexandre Leonelli
Department of Mechanical Engineering
University of California Santa Barbara
Santa Barbara, CA 93106
adleonelli@ucsb.edu

Eckart Meiburg
Department of Mechanical Engineering
University of California Santa Barbara
Santa Barbara, CA 93106
meiburg@engineering.ucsb.edu

ABSTRACT

Cohesive particles suspended in turbulence undergo a complex process of aggregation and breakup known in sediment transport as “flocculation.” Primarily investigated in homogeneous isotropic turbulence, less attention has been placed on the flocculation of cohesive granular materials in wall-bounded turbulence, where the flow is highly inhomogeneous. To address this, this work brings forward five particle-resolved direct numerical simulations of a turbulent channel flow laden with cohesive particles. Across each case, the strength of the cohesive force is increased. Statistics are collected so that a family tree of aggregation and breakup events may be constructed. A population balance equation (PBE) framework is employed, first to demonstrate how high fidelity data can inform model kernels, and secondly to reveal the coupled statistical trajectories of aggregates through size and physical space. When integrated over the full domain, the PBE is closed by aggregation and breakup alone, however this balance is shown to not hold locally in the wall-normal direction. By partitioning the channel into wall-normal subdomains, we identify regions of net production and depletion. This imbalance in aggregation and breakup must be compensated by the wall-normal advection of aggregates. This is shown to be the case, thus revealing a statistical circulation of aggregates through physical and size space that supports the local imbalance in aggregation and breakup: larger aggregates on average form in the channel center, migrate towards a wall and break into smaller fragments. These advect back to the channel center, where they aggregate once more, and begin the cycle again.

INTRODUCTION

The transport of cohesive particles by turbulent flows is central to many environmental and engineered systems (e.g. soil erosion, marine snow, microplastics, wastewater treatment, powder manufacturing). Turbulence plays a dual role in such transport processes; it acts to both promote aggregation by bringing particles together, while also enhancing breakup due to increased hydrodynamic stresses. This leads to an intricate process of aggregation and breakup known in the sediment transport community as “flocculation”. The flocculation process has typically been studied in homogeneous isotropic turbulence (HIT), where progress has been made both experimentally (Saha *et al.*, 2016; Hoffman & Eaton, 2023) and numerically (Zhao *et al.*, 2021; Yu *et al.*, 2024). Despite the need to inform modeling efforts of flocculation in wall bounded systems (Penaloza-Giraldo *et al.*, 2025*a*,*b*), to date limited focus has been placed on the transport of cohesive particles in wall bounded flows (e.g. Babler *et al.*, 2015; Afkhami *et al.*, 2015).

PHYSICAL CONFIGURATION

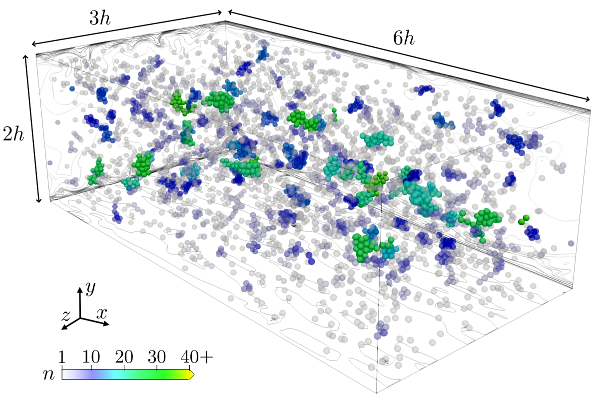

Figure 1. Schematic of the numerical domain displaying a snapshot of aggregates taken during the equilibrium period of $Co = 0.48$. Aggregates are colored by the number of constituent primary particles, n. Thin contours drawn on the walls show the streamwise velocity field. Flow is in the x-direction.

In this work, we consider a channel of half-height h and dimensions $(L_x, L_y, L_z) = (6h, 2h, 3h)$ filled with a suspension of $N_p = 3,841$ (1.5% volume fraction) neutrally buoyant cohesive particles of diameter $d = 2h/31$, immersed in a Newtonian fluid with dynamic viscosity μ_f and density ρ_f. The streamwise (x) and spanwise (z) directions are periodic, while the wall-normal direction is bounded by no-slip walls at $y = 0$ and $y = 2h$. An adaptive pressure gradient maintains a constant bulk velocity U and Reynolds number $Re = \rho_f U h/\mu_f = 2,800$. We use the cohesion model of Vowinckel *et al.* (2019) with a surface interaction distance $\lambda = 0.1d$ and cohesive number $Co = \max|F_{coh}|/\rho_f U^2 d^2$ denoting the ratio of maximum cohesive force to hydrodynamic inertial force. We consider five cases with $Co = \{0, 0.24, 0.48, 1.0, 1.5\}$, respectively.

Particles are initially randomly distributed, without overlap, throughout a fully developed single-phase turbulent channel flow, with each particle taking the mean linear and angular velocity of the fluid it replaces. The immersed boundary method based particle-resolved direct numerical simulation solver of Biegert *et al.* (2017) and Vowinckel *et al.* (2019) (based on Uhlmann (2005) and Kempe & Fröhlich (2012)) is then employed to solve the coupled fluid and particle momentum equations. A schematic of the computational domain is shown in figure 1 where a snapshot taken during the equilibrium period of the case $Co = 0.48$ shows the aggregates colored by the number of constituent particles, n.

FORMALISM

The population balance equation (PBE) (Smoluchowski, 1916, 1918) presents a well-established approach for modeling processes where mass is transferred between size classes by discrete aggregation or breakup events (e.g. bubbles, droplets, cohesive sediment). The PBE describes the evolution of the aggregate number density, $f(D,\mathbf{x},t)$, through $(D,\mathbf{x})$-space over time by an advection equation with source and sink terms accounting for discrete aggregation and breakup events. Note that $f(D,\mathbf{x},t)$ holds units of $(\text{length})^{1/4}$ and yields the total number of aggregates at time t, $N(t)$ when integrated over the full domain Ω and all sizes,

$$N(t) = \int_\Omega \mathrm{d}\mathbf{x} \int_0^\infty \mathrm{d}D f(D,\mathbf{x},t). \tag{1}$$

Written so that mass is explicit conserved, the mass-weighted PBE reads,

$$\frac{\partial f D^3}{\partial t} + \nabla \cdot \left(\mathbf{v} f D^3\right) = A_+ + A_- + B_+ + B_-, \tag{2}$$

where $\mathbf{v}(D,\mathbf{x},t)$ is the mean velocity of aggregates of size D in physical space, A_+ is the source of size D due to aggregation of smaller aggregates, A_- is the sink due to aggregation of size D itself, B_+ is the source due to fragmentation of larger aggregates yielding one or more fragments of size D, and finally B_- is the sink due to the breakup of size D itself. Hereafter, explicit dependence on $(\mathbf{x},t)$ is suppressed for brevity and all quantities are understood to depend on these variables unless explicitly stated, e.g. $S_i(D) = S_i(D,\mathbf{x},t)$. Expanded, the source and sink terms $S_i \in \{A_+, A_-, B_+, B_-\}$ read,

$$A_+(D) = \frac{D^3}{2} \int_0^D \int_0^D \mathrm{d}D_1 \mathrm{d}D_2 K(D_1,D_2)\,\delta(D^3 - D_1^3 - D_2^3), \tag{3}$$

$$A_-(D) = -f(D)\,D^3 \int_0^\infty \mathrm{d}D' f(D')\,h(D,D')\,q_a(D,D'), \tag{4}$$

$$B_+(D) = D^3 \int_D^\infty \mathrm{d}D_p f(D_p)\,g_b(D_p)\,q_b(D_p,D), \tag{5}$$

$$B_-(D) = -D^3 f(D)\,g_b(D), \tag{6}$$

where $K(D_1,D_2) = f(D_1)f(D_2)h(D_1,D_2)q_a(D_1,D_2)$, $h(D_1,D_2)$ is the collision rate of sizes D_1 and D_2, $q_a(D_1,D_2)$ is the probability of an aggregate forming by a collision, $g_b(D_p)$ is the breakup rate of size-D_p parent aggregates, $q_b(D_p,D)$ is the fragment size distribution, and $\delta(D^3 - D_1^3 - D^3)$ is the Dirac delta function, used to explicitly restrict aggregation events to mass-conserving pairs. With this formulation, we assume that aggregation and breakup events are binary (one parent producing two children for breakup and two parents producing one child for aggregation) and will carry this assumption for the rest of the work.

Integrating equation (2) over the periodic streamwise and spanwise directions and averaging over the equilibrium period yields the plane- and time-averaged PBE,

$$\frac{\partial}{\partial y}\left(\overline{vf}D^3\right)(D,y) = \overline{A_+}(D,y) + \overline{A_-}(D,y) + \overline{B_+}(D,y) + \overline{B_-}(D,y), \tag{7}$$

where, $\overline{\cdot}$, signifies a plane-time averaged quantity dependent only on (D,y). Here it is important to emphasize that the advective term permits aggregation and breakup to be locally imbalanced in y, i.e. $\sum \overline{S_i}(D,y)$ is not constrained to vanish.

Additionally integrating over the wall-normal direction yields the bulk PBE,

$$0 = \overline{\overline{A_+}}(D) + \overline{\overline{A_-}}(D) + \overline{\overline{B_+}}(D) + \overline{\overline{B_-}}(D), \tag{8}$$

where the advective term is removed by the boundary conditions in the wall-normal direction, since aggregates can not penetrate the walls. Here, $\overline{\overline{\cdot}}$ signifies a volume and time averaged quantity dependent only on D.

RESULTS

In this work, we consider an aggregate of size n to be a grouping of n particles in which any two are linked by a chain of neighbors separated by a surface distance less than λ. In addition to the number of constituent particles, an aggregate may be characterized by the diameter of a sphere with equal volume to the solid volume of the aggregate $D = n^{1/3}d$. This equivalent diameter is chosen since the aggregate volume, D^3, is conserved across aggregation and breakup events.

The simulations first advance through a transient phase of net aggregate growth before reaching an equilibrium in which aggregation and breakup globally balance. The total number of aggregates, $N(t)$, is shown for each Co case in figure 2. Here, $N(t)$ relaxes from its initial value, $N(t=0) = N_p$, to an equilibrium value, N_{eq}. Consistent with observations in HIT and cellular flows (Zhao *et al.*, 2020, 2021), this relaxation is exponential and can be fit with,

$$N(t) = (N_p - N_{eq})e^{-t/\tau} + N_{eq}, \tag{9}$$

where, τ, the agglomeration time constant, and N_{eq} serve as fitting parameters. The time to reach equilibrium, t_{eq}, can then be taken as the time it takes $N(t)$ to decay to within 1% of N_{eq},

$$t_{eq} = -\tau \ln\left(\frac{0.01}{N_p/N_{eq} - 1}\right). \tag{10}$$

Figure 2 also shows the fits of equation (9) as dotted lines of the same color as the data. t_{eq} is superimposed as a circular marker along the fitted curve and is found to increase with

Co. Unlike HIT, however, the relaxation to equilibrium is dependent on the wall-normal coordinate, with the near-wall region equilibrating more rapidly than the channel center due to higher shear rates, as discussed in Leonelli & Meiburg (2026).

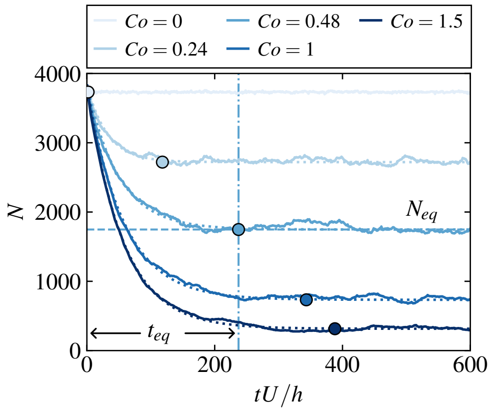

Figure 2. Total number of aggregates N over time t (solid lines) for each *Co* case. Exponential fits of equation 9 are shown as dotted lines of matching color. For each case, the time to reach equilibrium, t_{eq} (equation 10) is displayed as a circular marker along each fit. The equilibrium number of aggregates, N_{eq} and t_{eq} are additionally shown as a horizontal dash and vertical dashed-dotted line and respectively labeled for $Co = 0.48$.

Within the equilibrium period, statistics are sampled every $0.001h/U$, ensuring that fewer than 1% of aggregation and breakup events are missed, and so allowing for the computation of an aggregate family tree spanning the entire sampling window. The total sampling duration is chosen to span at least 10 correlation times of $N'(t) = N(t) - N_{eq}$ for each case, ensuring statistical convergence. Error bars throughout denote 95% confidence intervals.

The bulk mass-weighted aggregate number density, $(D/d)^3\overline{\overline{f}}$ is computed using 18 bins in D, with the first 4 linearly spaced and the remainder logarithmically spaced to balance the discrete nature of small aggregates with the sparse statistics at larger sizes. The result is shown in figure 3 as a function of normalized aggregate size, D/d, on a logarithmic x-axis.

Unsurprisingly, increasing *Co* promotes the formation of larger aggregates. While $(D/d)^3\overline{\overline{f}}$ is monotonically decreasing for $Co \leq 0.24$, the distributions for $Co \geq 0.48$ develop an approximately log-normal region for $D/d > 3^{1/3}$. Log-normal fits for $Co \geq 0.48$, made neglecting the region $D/d \leq 3^{1/3}$, are shown as solid lines in both the main panel and inset. This emergence of a non-monotonic number density is revisited below in the context of aggregation and breakup statistics, where it is shown to reflect the growth of an intermediate range of aggregate sizes where aggregation and breakup establish a statistical circulation of aggregate mass in size-space that excludes the smallest aggregate sizes.

Informing PBE Models

Accurate parameterization of the aggregation and breakup kernels is essential for the performance of PBE based sediment transport models. Exploiting the detailed statistics on

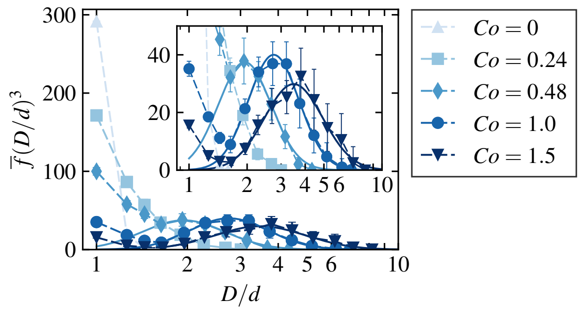

Figure 3. Mass-weighted aggregate number density, $(D/d)^3\overline{\overline{f}}$, versus aggregate size $D/d = n^{1/3}$ for all *Co*. The x-axis is logarithmically scaled. Log-normal fits for $Co \geq 0.48$, obtained over $D/d > 3^{1/3}$, are shown as solid lines in the main panel and inset. Error bars denote 95% confidence intervals, which may appear missing if smaller than the marker.

aggregation and breakup provided by the simulations allows for explicit measurement of, for example, the breakup rate, g_b, and fragment size distribution q_b. The bulk breakup rate, $\overline{\overline{g_b}}$, computed over the sampling interval, is shown in figure 4(a), where error bars denote a 95% confidence interval in this and subsequent figures. Intuitively, $\overline{\overline{g_b}}$ decreases with increasing cohesive strength *Co*, reflecting the enhanced stability of aggregates held together by stronger bonds. Notably, the breakup rate exhibits a scaling with effective aggregate surface area, $\propto D^2$. Power-law fits of the form $y = Ax^2$ are shown for each case in figure 4(a). Rescaling by cohesive strength collapses the data, with $\overline{\overline{g_b}}Co \propto D^2$, as shown in figure 4(b) where it is accompanied by a power-law fit of the collapsed data and suggests that simplified models for $\overline{\overline{g_b}}$ require only a single functional form, independent of *Co*. The scaling with aggregate surface area holds primarily at large D/d, where the notion of an effective diameter remains meaningful. The compensated breakup rate, $\overline{\overline{g_b}}D^{-2}Co$, is shown in figure 4(c) to highlight this convergence.

To further characterize the breakup process, we examine the bulk parent-child fragment distribution across breakup events. The probability density function (PDF) of fragment sizes, computed from $q_b(D_p, D_c)$, is expressed in terms of the child-parent volume ratio $D_c^3/D_p^3 \in (0,1)$ and shown across 9 bins in figure 5. To suppress the highly discrete contributions of small aggregate breakup, we only consider events with $D_p/d > 9^{1/3}$. By mass conservation, the distribution is symmetric about $D_c^3/D_p^3 = 0.5$. The PDF is strongly peaked near the extremes, indicating that breakup predominantly produces one large and one small fragment, consistent with an erosional breakup mechanism. Notably, the distribution is largely independent of *Co*, in agreement with observations in 2D interfacial turbulence (Qi *et al.*, 2025), but not previously reported for 3D wall-bounded flows. The beta distribution,

$$\overline{\overline{q_b}}(D_p, D_c) = 2D_c^{3(\alpha-1)}\left(D_p^3 - D_c^3\right)^{\alpha-1} D_p^{-6(\alpha-1)-3} / B(\alpha,\alpha) \tag{11}$$

is commonly employed to capture such fragment distributions for flows of bubbles and droplets. Here we borrow the formulation of Chan *et al.* (2021) in which B is the beta distribution and α is the single free parameter. Fitting the accumulated data for all *Co* yields $\alpha = 0.4$ with the resulting PDF shown as

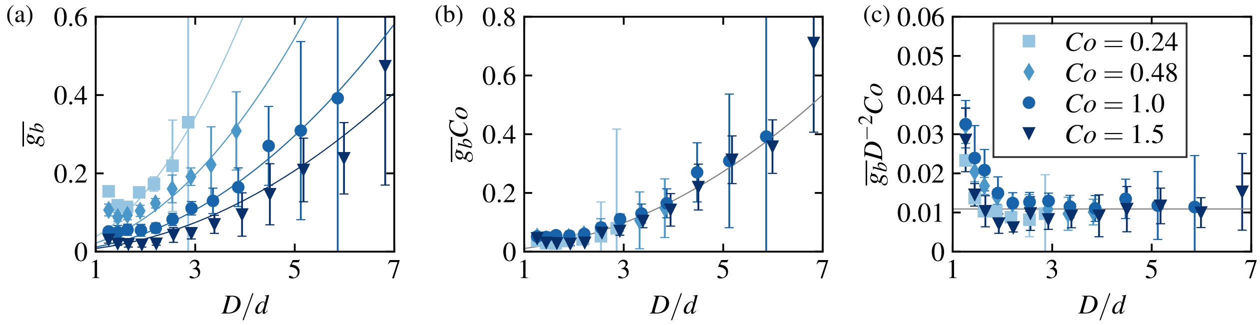

Figure 4. (a) Breakup rate, $\overline{\overline{g_b}}$, versus normalized aggregate size D/d. (b) Rescaled by Co to demonstrate collapse. (c) Compensated by $D^{-2}Co$ to highlight the D^2 scaling. Power law fits $y = AD^2$ are shown as solid lines in each panel. Error bars denote a 95% confidence interval.

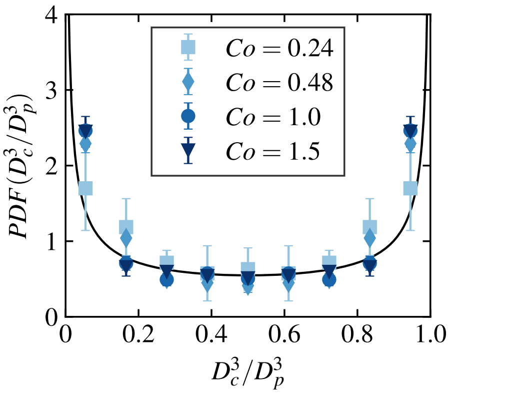

Figure 5. Probability density function (PDF) of child-to-parent fragment volume ratios, D_c^3/D_p^3, for each $Co > 0$. Only breakup events where $D_p/d > 3$ are considered. Equation (11) is fit to the data for all Co and shown as a black line.

a black line in figure 5. The agreement between (11) and the data is good, demonstrating its viability as a model fragment size distribution to parameterize the breakup kernels B_+ and B_-.

Similar analysis may be conducted for the aggregation kernels but is omitted here for brevity. It is also important to note that the results presented are likely specific to the flow and geometry considered and that a broader body of work is needed to assess the robustness of the observed scaling laws.

Global PBE closure

When considering the full domain volume, aggregation and breakup must balance, at every D as stated in equation (8). Note that this is true only in equilibrium, and so also serves as a measure of a statistically steady state. Indeed, the bulk-averaged aggregation source and sink terms, and their sum $\overline{\overline{Q}} = \sum_i \overline{\overline{S_i}} = \overline{\overline{A_+}} + \overline{\overline{A_-}} + \overline{\overline{B_+}} + \overline{\overline{B_-}}$ are displayed in figure 6 and demonstrate the required closure across size space ($\overline{\overline{Q}}(D,y) \approx 0 \forall D$). Here, we select $Co = 0.24$ and $Co = 1.0$ to be representative of the behavior of lower and higher Co. Firstly, at $D/d = 1$ (monomers), aggregates can only be produced by breakup and depleted by aggregation, thus $B_+ = -A_-$. At $D/d > 1$ A_+ and B_- become active as aggregates of some size D/d can now be created or depleted by both aggregation and breakup.

Before proceeding, we briefly revisit the log-normal distribution in the aggregate number density for $Co \geq 0.48$. It was mentioned in the discussion surrounding figure 3 that the non-monotonic dependence on D/d was a result of differences in the source and sink behavior of aggregation and breakup across size space which in turn varies with Co. Indeed, if one closely inspects figure 6(a,b) we can discern two distinct regions (omitting D/d = 1) in D-space. In the first region type, colored red, the net role of aggregation is as a source of size D aggregates, $\overline{A_+}(D) + \overline{A_-}(D) > 0$, meaning that more mass is incoming to size D due to the coalescence of smaller aggregates than is outgoing due to the aggregation of size D itself. Forcibly, breakup maintains the opposite direction and magnitude of mass transfer as, $\overline{B_+}(D) + \overline{B_-}(D) < 0$, indicating that more mass is leaving size D due to breakup into smaller aggregates than is incoming due to breakup events resulting in at least one size D fragment. The opposite, however can also occur, where $\overline{B_+}(D) + \overline{B_-}(D) > 0$ and $\overline{A_+}(D) + \overline{A_-}(D) < 0$. This second region type is colored blue.

Noticeably, no blue region is present at low Co, thus aggregation always acts as a source across all D/d and breakup a sink. There is therefore always a statistical pathway to the primary particle. This is not the case for $Co \geq 0.48$, as demonstrated by $Co = 1.0$ shown in figure 6(b,c). Breakup acts as a net source and aggregation a net sink for the intermediate D/d included in this blue region. Because of this, incoming mass from larger aggregates ($\overline{B_+}$) is statistically redistributed upscale due to aggregation ($\overline{A_-}$) rather than passed downscale by further breakup ($\overline{B_-}$). This cycle in size-space manifests as a non-monotonic aggregate number density, which in the present cases appears to be log-normal when mass-weighted.

Local PBE closure

Given the global closure of the PBE across size space, as required by equation (8) and demonstrated above, we now ask whether this closure holds locally in the wall-normal direction, where the advective term permits $\overline{Q}(D,y) \neq 0$. To investigate this, the channel is partitioned into 62 wall-normal subdomains of height $\Delta y = d/2$, and the terms of (7) are evaluated within each.

The resulting net source term, $\overline{Q}(D,y)$ (solid line), is shown over half the channel, $y/h \in [0,1]$ (exploiting symmetry about $y = h$) for three size classes, $n = 1$, $n = 2,3$, and $n > 3$ in figure 7 for $Co = 0.48$ and $Co = 1.0$. We consider these subsamples of n individually since aggregation and breakup conservatively redistribute mass across sizes (i.e. a breakup event at size $n = 3$ will be balanced by the breakup source term at

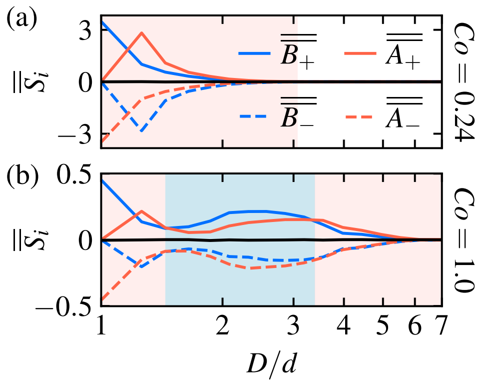

Figure 6. Bulk aggregation and breakup source and sink terms, equations (3-6), over normalized aggregate size D/d for (a) $Co = 0.24$ and (b) $Co = 1.0$. Omitting $D/d = 1$, regions where net aggregation acts as a source $\overline{A_+}(D) + \overline{A_-}(D) > 0$ and net breakup a sink $\overline{B_+}(D) + \overline{B_-}(D) < 0$ are highlighted in red while the opposite case is highlighted in blue.

$n = 1$ and $n = 2$ in the same y bin), such that

$$\int_0^\infty \mathrm{d}D\overline{Q}(D,y) = 0. \tag{12}$$

Figure 7, clearly shows that $\overline{Q}(D,y) \neq 0$ in general, indicating that aggregation and breakup are not locally balanced in the wall-normal direction. Regions of net aggregate production and depletion are highlighted by a gray shading between 0 and $\overline{Q}$.

For $Co = 0.24$, (panels (a-c)), there is net production of monomers ($n = 1$, $\overline{Q} > 0$) near the wall, and net depletion ($\overline{Q} < 0$) in the channel center. While $\overline{Q}$ alone does not distinguish between aggregation and breakup contributions, monomers cannot undergo further breakup and are not formed by aggregation. Therefore, their net production near the wall implies that breakup dominates over aggregation there, with the opposite behavior in the channel center. This suggests a statistical cycle in which monomers are preferentially generated near the wall and depleted by aggregation toward the channel center.

For larger aggregates ($n = 2,3$ and $n > 3$, panels (b) and (c)), the structure of $\overline{Q}$ is reversed relative to the monomers. Net production occurs in the channel center, with net depletion near the walls. A similar trend is observed for $n > 3$ at $Co = 1.0$ (panel (f)). However, unlike the $Co = 0.24$ case, the $n = 2,3$ class at $Co = 1.0$ (panel (e)) exhibits behavior more similar to $n = 1$, which maintains a consistent structure across all Co. These regions of net production and depletion must be balanced by the advective transport of aggregates $\partial_y(\overline{vfD^3})$, shown as the dashed line in figure 7. As expected from (7), the agreement between these terms is good.

Finally, examining either the advective flux or $\overline{Q}$ in (D,y) space reveals the full statistical trajectories of aggregates evolution at equilibrium. We illustrate this using the wall-normal advective flux for $Co = 1.0$ in figure 8, from which a statistical circulation, also observed in all other Co, can be constructed. The colormap is chosen so that regions of advective inflow are shown in blue, while outflow regions are shown in red.

Beginning with small, near wall aggregates in region 1, aggregates exhibit a net advective flux away from the wall toward the channel center, flowing into region 2. There, the wall-normal transport leads to an accumulation of mass ($\partial_y\overline{vfD^3} < 0$). Since region 2 is bounded by advective outflow below, the symmetry plane above, and $n = 1$ in size space, this excess mass must be transferred upscale by aggregation into region 3 (recall $\overline{Q} = \partial_y(\overline{vfD^3})$).

Region 3 is thus characterized by net production through aggregation. As advection redistributes mass only in the wall-normal direction, the only permissible transport is from region 3 into the near-wall region 4. In this region, advection cannot remove mass due to the opposing fluxes from above and the presence of the wall below. Consequently, the near-wall aggregate mass that accumulates at the largest sizes must be redistributed through breakup to smaller aggregates, returning to region 1 and closing the cycle.

In summary, a statistical cycle emerges; small aggregates are preferentially produced near the wall by breakup, advected toward the channel center ($1 \to 2$), grow through aggregation ($2 \to 3$), are transported back toward the wall ($3 \to 4$), and undergo breakup once more ($4 \to 1$).

CONCLUSION

In this work, we have investigated five PR-DNS of turbulent channel flow laden with finite-sized, neutrally buoyant, cohesive particles, spanning five cohesive strengths, Co. Using a PBE framework, we demonstrate how such simulations can potentially be upscaled to inform PBE-based sediment transport models, analogous to approaches used for droplet-laden and bubbly flows.

Within this framework, we find that the global breakup rate, $\overline{\overline{g_b}}(D)$, collapses across Co and is well described by a power law, $\sim D^2$, indicating that, within the present flow and geometry, the global breakup rate can be modeled by a single function scaling with the effective aggregate surface area for all $Co > 0$. Further examination of the breakup kernel reveals that breakup is predominantly erosional, typically producing one small and one large fragment.

Exploiting the PBE analytically, we show that aggregation and breakup must balance globally, but, nontrivially, it does not balance locally in the wall-normal direction. Instead, equilibrium is maintained through spatially separated regions of net aggregate production and depletion. Closure of the PBE is recovered through the inclusion of size-dependent wall-normal advective transport.

Finally, analysis in (D,y) space reveals a statistical cycle: small aggregates are net produced near the wall, advected towards the channel center where they grow through aggregation, transported back toward the wall, and subsequently broken down, re-entering the cycle.

Looking forward, it will be important to assess how closely individual aggregates follow these statistical trajectories. In particular, Lagrangian statistics, along with more detailed understanding of the three-dimensional organization of aggregation and breakup relative to turbulent flow structures, will likely drive further insight into the wall bounded flow of cohesive granular materials.

ACKNOWLEDGEMENTS

A.D.L. and E.M. would like to thank Lukas Widmer for aiding in the development of the PBE analysis and Prof. Filippo Coletti and Dr. Ronald Chan for many constructive discussions. A.D.L. and E.M. are grateful for financial support from the Geological Survey of Israel, the Army Corps of Engineers through grant No. W912HZ22C0037, the Army Re-

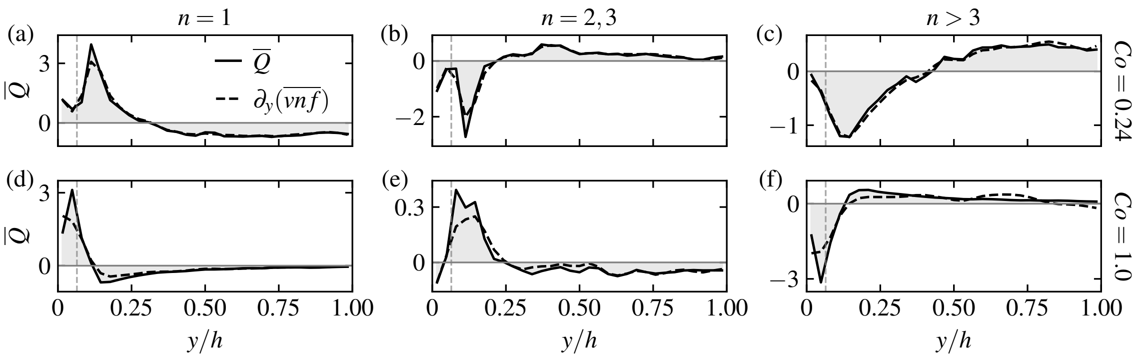

Figure 7. Net aggregation and breakup source $\overline{Q}(n,y)$ (solid) and advective aggregate mass flux $\partial_y(\overline{vfD^3})$ (dashed) across the half channel height, $y/h \in [0,1]$ for three size classes, $n=1$, $n=2,3$, and $n>3$ (columns) for $Co=0.24$ (row 1) and $Co=1.0$ (row 2).

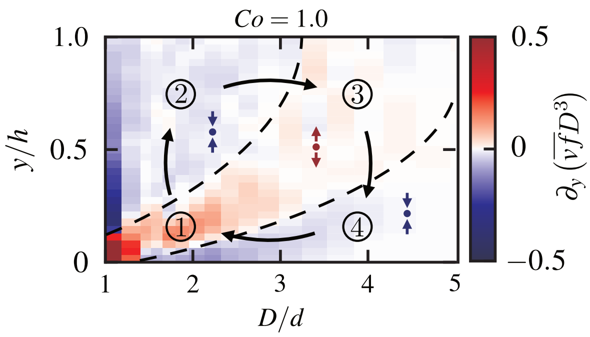

Figure 8. Wall-normal advective transport of aggregates, $\partial_y(\overline{vfD^3})$ in (D,y) space for $Co=1.0$. Dashed lines aid in distinguishing between regions of $\partial_y(\overline{vfD^3}) > 0$ (red) and $\partial_y(\overline{vfD^3}) < 0$ (blue). The annotations within the figure are used to describe the cyclic transfer of mass through regions 1-4 in the text. Symbols with vertical arrows show the divergence of $\overline{vfD^3}$ to compliment the red and blue coloring.

search Office through grant No. W911NF-23-2-0046, and from the Rosen Center for Advanced Computing through computational resources.

REFERENCES

Afkhami, M., Hassanpour, A., Fairweather, M. & Njobuenwu, D.O. 2015 Fully coupled LES-DEM of particle interaction and agglomeration in a turbulent channel flow. *Comput. Chem. Eng.* **78**, 24–38.

Babler, M.U., Biferale, L., Brandt, L., Feudel, U., Guseva, K., Lanotte, A.S., Marchioli, C., Picano, F., Sardina, G., Soldati, A. & Toschi, F. 2015 Numerical simulations of aggregate breakup in bounded and unbounded turbulent flows. *J. Fluid Mech.* **766**, 104–128.

Biegert, E., Vowinckel, B. & Meiburg, E. 2017 A collision model for grain-resolving simulations of flows over dense, mobile, polydisperse granular sediment beds. *J. Comput. Phys.* **340**, 105–127.

Chan, W.H.R., Johnson, P.L. & Moin, P. 2021 The turbulent bubble break-up cascade. Part 1. Theoretical developments. *J of Fluid Mech.* **912**, A42.

Hoffman, D.W. & Eaton, J.K. 2023 Experimental investigation of particle aggregation in a humid and turbulent environment. *Int. J. Multiph. Flow* **163**, 104423.

Kempe, Tobias & Fröhlich, Jochen 2012 An improved immersed boundary method with direct forcing for the simulation of particle laden flows. *J. of Comput. Phys.* **231** (9), 3663–3684.

Leonelli, A. & Meiburg, E. 2026 On the effects of anisotropy on the flocculation of cohesive particles in turbulence. *Acta Mech.* **237** (4), 1699–1713.

Penaloza-Giraldo, J.A., Yue, L., Hsu, T.-J., Vowinckel, B., Manning, A.J. & Meiburg, E. 2025*a* A Modeling framework for flocculated cohesive sediment transport in the current bottom boundary layer. *Adv. Water Resour.* **195**, 104857.

Penaloza-Giraldo, J.A., Yue, L., Hsu, T.-J., Vowinckel, B., Manning, A.J. & Meiburg, E. 2025*b* A numerical modeling framework for flocculation and cohesive sediment transport in the wave bottom boundary layer. *J. Geophys. Res. Oceans* **130** (11), e2025JC022373.

Qi, Y., Shin, S. & Coletti, F. 2025 Breakup and coalescence of particle aggregates at the interface of turbulent liquids. *J of Fluid Mech.* **1021**, A49.

Saha, D., Babler, M.U., Holzner, M., Soos, M., Lüthi, B., Liberzon, A. & Kinzelbach, W. 2016 Breakup of Finite-Size Colloidal Aggregates in Turbulent Flow Investigated by Three-Dimensional (3D) Particle Tracking Velocimetry. *Langmuir* **32** (1), 55–65.

Smoluchowski, M.V. 1916 Drei Vortrage uber Diffusion, Brownsche Bewegung und Koagulation von Kolloidteilchen. *Phys. Z.* **17**, 557–585.

Smoluchowski, M.V. 1918 Versuch einer mathematischen theorie der koagulationskinetik kolloider lážĚosungen. *Z. Phys. Chem.* **92**, 129–168.

Uhlmann, Markus 2005 An immersed boundary method with direct forcing for the simulation of particulate flows. *J. of Comput. Phys* **209** (2), 448–476.

Vowinckel, B., Withers, J., Luzzatto-Fegiz, P. & Meiburg, E. 2019 Settling of cohesive sediment: particle-resolved simulations. *J. Fluid Mech.* **858**, 5–44.

Yu, X., Balachandar, S., Smith, J. & Manning, A.J. 2024 Flocculation dynamics of cohesive sediment in turbulent flows using cfd-dem approach. In *Sediment Transport Research - Further Recent Advances*. IntechOpen.

Zhao, K., Pomes, F., Vowinckel, B., Hsu, T.-J., Bai, B. & Meiburg, E. 2021 Flocculation of suspended cohesive particles in homogeneous isotropic turbulence. *J. Fluid Mech.* **921**, A17.

Zhao, K., Vowinckel, B., Hsu, T.-J., Köllner, T., Bai, B. & Meiburg, E. 2020 An efficient cellular flow model for cohesive particle flocculation in turbulence. *J. Fluid Mech.* **889**, R3.